Broadband measurements of the surface impedance in ferromagnetic wires as a boundary condition for scattering problems

Azim Uddin[1], Faxiang Qin[1,*], Diana Estevez[1,2], Konstantin Gorbatov[3], Yujie Zhao[4], and Dmitriy Makhnovskiy[5]

[1]*Institute for Composites Science Innovation (InCSI), School of Materials Science & Engineering, Zhejiang University, 38 Zheda Road, Hangzhou, 310027, China.*

[2]*Ningbo Innovation Centre, Zhejiang University, 1 South Qianhu Road, Ningbo, 315100, China.*

[3]*Lisi Aerospace, 38 Butlers Leap, Rugby, Warks CV21 3RQ, England.*

[4]*School of Physics and Astronomy, University of St. Andrews, Fife KY16 9SS, Scotland.*

[5]*Sensing Materials Technology Ltd, 44 St. Michael's Close, Plymouth, Devon PL1 4RX, England.*

[*] Corresponding author: faxiangqin@zju.edu.cn

Abstract

In the cm-wave range, the skin depth is comparable to the micron radius of ferromagnetic wires and thus their magnetic and conductive properties will influence the scattered electromagnetic field. Solving the scattering problem by considering the complicated internal magnetic structure of the wire becomes unpractical. There is a need to develop hybrid methods when the external problem of scattering on an inclusion is solved together with the experimental impedance conditions on its surface. Herein, we propose an accurate broadband impedance measurement technique operating up to 15 GHz. The PCB measurement and calibration cells designed in this work allow flexibility in choosing external stimuli such as magnetic field, tensile stress, and heat. The experimental impedance can be then used as the boundary condition in electromagnetic simulations making it possible to model, predict and design wire-based composites using numerical solvers such as CST Studio Suite.

Keywords: Impedance boundary condition; Ferromagnetic microwires; Network calibration; De-embedding; Microwave scattering; PCB cells.

1. Introduction

Dynamic magnetic behaviour through magnetoimpedance (MI) effect [1] is an essential property to characterize the microwave response of different materials such as ferromagnetic microwires [2-6], ribbons [7], and thin films [8-10]. Apart from fundamental research interest, in the technological context materials exhibiting a large MI effect arise as field/stress-sensitive sensors that can be integrated into a wide range of devices [11-16]. Special emphasis has been placed on Co-based and Fe-based glass-coated microwires. The thin glass shell ($2 - 15$ microns) along with the magnetostriction (positive or negative) of the core alloy (diameter $5 - 30$ microns) determine their unique magnetic anisotropic and mechanical properties. The technology of continuous casting of such wires makes it possible to produce highly-flexible threads of kilometre length [17]. These features allow them to be used as functional fillers in composite materials to introduce electromagnetic functionalities in the microwave range (ultra-high frequency UHF and super high frequency SHF bands), such as field/stress tunability, cloaking, absorption and shielding [18-24]. Such plethora of functional materials and their increasing trend towards operating at broader bandwidth stimulate the development of accurate measurement techniques to characterize their MI and microwave behaviour. The most commonly used methods are based on shorted coaxial transmission lines [25-27], microstrip transmission lines (MTLs) and coplanar waveguides (CPWs) etched on printed circuit boards (PCB) [28-32] aided by vector network analysers (VNA). In the shorted coaxial lines, one end of the microwire is connected to the inner conductor, while the other end is connected to the ground of the coaxial cap. The alignment of the sample along the axis will determine the measurement accuracy. Except for testing under magnetic field, measurements with sample stretching or heating are hardly possible in such coaxial cells. MTLs consist of a metal-backed substrate of relative permittivity ε_r on top of which is a metal strip with its width determined by the characteristic impedance of the line [33]. The sample is usually mounted on the surface of a PCB in the gap between two aligned microstrips and connected to them by soldering or conducting painting/glue. This method works for elongated samples of various geometries (wire, film, or ribbon), which can be considered as a continuation of a microstrip waveguide, although with a different characteristic impedance. Mounting the sample on the surface of PCB allows the application of external stimuli, including magnetic field, heat, and tensile stress. Meanwhile, the CPW PCB cells have an additional ground plane on the side of the microstrips that improves signal integrity at higher frequencies. This plane is also convenient for adding shunt surface elements, such as SHORT and LOAD terminations, which can be used for

calibration of the microstrip network. The CPW cells are suitable for another measurement scheme where a thin and sufficiently wide sample (film or ribbon) is placed over the continuous strip, covering only its central segment. Direct electrical contact with the strip is excluded by introducing a subtle gap or isolating layer. The parameter of interest is no longer the impedance of the sample itself, but its magnetic and dielectric properties, determined indirectly through the measurement of S-parameters of the loaded waveguide segment [28].

VNA, coaxial cables, non-coaxial strips on PCB, and a non-lumped sample constitute a cascaded network that requires a multi-stage calibration procedure. The ultimate goal is to extend the reference plane directly to the sample. VNA and the cables can be calibrated using the standard 12-term error correction model with the coaxial SHORT-OPEN-LOAD-THRU (SOLT) terminations. The strip waveguides must be de-embedded based on different methods [28,30,31,34]. In turn, an elongated sample over a continuous ground (or segment of a loaded strip) constitutes a structure which waveguide properties must be considered when calculating material parameters from the S-parameter measurements. The principles of multi-stage calibration have already been implemented for thin film samples, where ferromagnetic resonance (FMR) and permeability dispersion were of primary interest [28,31]. The study of Bilzer *et al.* [28] is closely related to the method developed in our present work since the waveguide properties of the loaded CPW segment were explicitly revealed there. The measurements were carried out up to 14 GHz, which is of interest for microwave scattering applications. However, this method requires an additional reference measurement when the film sample is removed leaving a continuous strip, and thus cannot be applied to a wire sample. In another method proposed by Gonzalez *et al.* [31], a thin film sample was electrically attached to microstrips on the PCB surface. It was assumed that the per-unit-length resistance and inductance (used as indicative parameters characterising FMR), could be derived from the measured characteristic impedance and propagation exponent. However, it remained unclear how the shunt capacitance and conductance (per unit length) were estimated, which are required to solve the corresponding equations. The maximum measurement frequency was up to only 3 GHz, which, given the sample length used (11 mm), does not allow to judge the accuracy of the phase distortion compensation along the sample. A radical decrease in sample length enables considering the sample as a lumped element without a phase incursion even at higher GHz. Such measurements have been performed with short wires connected at the end of an open coaxial connector between the core and the ground shell [35,36]. However, in very short samples, the magnetic domain structure at the ends might significantly change both the magnetostatic and high-frequency properties. Moreover, due to open-end parasitic capacitance

and radiation losses (which are not included in the calibration), the accuracy of impedance measurements will deteriorate.

In this work, we develop a broadband method for measuring accurately the field and stress dependencies of the surface impedance in ferromagnetic wires. The measurements in the frequency range up to 15 GHz were performed on MTL cells. In contrast to Bilzer and Gonzalez [28,31], the part of the network formed by the microstrip and the coaxial connector on PCB was not assumed to be ideal. Its 3-term model was created using a calibration cell where three reflection coefficients were measured from identical microstrips with surface mount SOL terminations. Touchstone S1P files containing the reflection coefficients were then created for such microstrips and uploaded to the VNA for automatic de-embedding. The phase distortion along the sample was compensated numerically using a phase unwrapping technique. The measured impedance dispersions were fitted with multi-pole dispersion models available in CST Studio Suite and followed the Kramers-Kronig relations. Recently, it has been shown that conventional impedance models [37,38] cannot accurately reproduce impedance response in the transition from MHz to GHz [39]. Thus, these models have limited practical value in modelling the microwave response in free space. However, with our reliable impedance measurement technique, it would be possible to realise a hybrid approach [40], where the experimental surface impedance is used to numerically solve the scattering problem of an individual wire inclusion without considering its complex magnetic domain structure [41]. Such approach will enable designing wire-filled composites with desirable microwave properties and predict their microwave response under external stress/temperature/field stimuli.

2. PCB measurement and calibration cells

We have explored two types of PCB measurement cells, straight and dogbone, shown in Fig. 1. A cell consists of two microstrips on one side of the board, and a continuous copper ground plane on the opposite side (Fig. 1a). The microstrips are soldered to SMA connectors at the edge of the PCB. A straight wire sample is placed in the gap between the microstrips and connected to them with conductive silver paint, which solidifies without additional heating. Rogers's composite materials [42] are widely used for high-frequency PCB designs due to their stable and isotropic dielectric properties with negligible temperature drift and low loss. Our boards were made of RO4003-C composite with a thickness of 0.812 mm and dielectric constant $D_k = 3.55$ over a broad frequency range and low dielectric losses. To calculate the microstrip width, we used the online microwave calculator available on Rogers' website. For the chosen D_k and thickness, the width of the microstrips was calculated as 1.742 mm,

providing a characteristic impedance close to 50 Ω over the whole frequency range. Further rules for designing waveguide structures can be found in [33].

A simpler straight PCB cell allows the application of external stimuli such as magnetic field and heating (Fig. 1b). Heating can be realized by local blowing of samples with hot air. Typical boards can withstand prolonged heat up to 200 degrees. Ceramic substrates have practically no temperature restrictions. The main problem remains the removal of heat from the rest of the board, where the coaxial connectors are located. The easiest way to control the temperature is with thermocouples at one or more reference points, where it can be measured with an accuracy of fractions of a degree. The closeness of the wire temperature to those measured at the reference points will be guaranteed by the uniformity of the blowing flow, the incomparably greater heat capacity of the board, and the high thermal conductivity of the wire. The dogbone cell (Fig. 1c) has protrusions for gripping by the clamps of the stress machine that allows the transfer of tensile stress to the sample through the elastic deformation of the PCB. After the sample was connected to the microstrips, it can be additionally glued to the board for more efficient stress-transfer. Simultaneously with stretching, the sample can be exposed to magnetic field and heating. Each cell type has a fixed microstrip length, and the gap between microstrips can be varied to accommodate samples of varying lengths (10 and 20 mm). The length of the sample should be much longer than the end segments involved in the connection to the microstrips ($1 - 2$ mm each from each side). Measurement of shorter wire samples would solve the problem of phase incursion along them [35,36]. However, it may introduce significant distortions due to the magnetic domains at the wire ends, as well as increasing uncertainty in the length outside the contact pads.
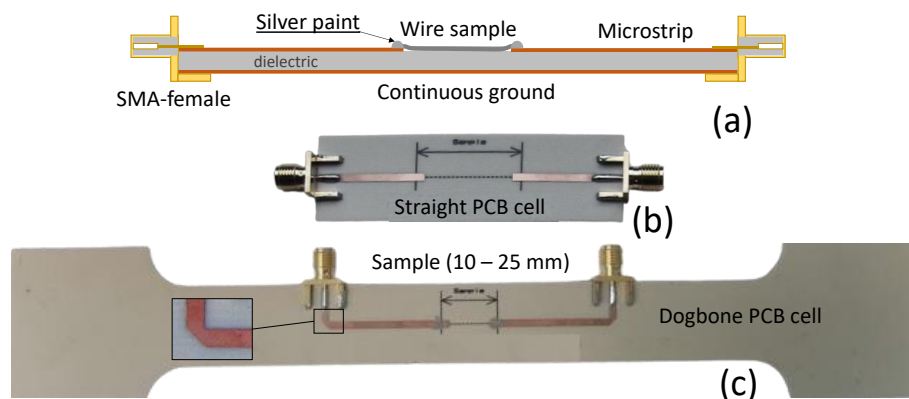

Fig. 1. PCB cells used for the impedance measurements (a) schematic diagram of the PCB cell; (b) straight cell; (c) dogbone cell

158 Phase and amplitude distortions, including multiple reflections introduced by the
159 microstrips, will be compensated by de-embedding based on the 3-term error correction model.
160 This method requires three reflection coefficient (S_{11}) measurements from the microstrip with
161 SHORT, OPEN, and LOAD (50 Ω) surface mount terminations (SOL). Further details are
162 discussed in the following section. To provide such measurements, calibration cells were
163 developed for the straight (Fig. 2a) and dogbone (Fig. 2b) geometries. The microstrips on the
164 calibration cells were reproduced exactly as those on the measurement cells. OPEN termination
165 is just the open end of the microstrip. Up to several GHz, such termination will behave as an
166 ideal reflector with $S_{11O} = 1$ (linear magnitude). However, in the vicinity of 6 GHz, a
167 resonance was observed, indicating the need for a more accurate model. Apparently, already
168 starting from this frequency, it is necessary to consider the terminal parasitic capacitance, as
169 well as radiation losses from the open end which result in an effective impedance in series with
170 the capacitance. SHORT is a 0.3 mm via (copper plated hole) connecting the microstrip end
171 with the continuous ground on the opposite side of the board. This termination will behave like
172 a true reflector with $S_{11S} = -1$ (linear magnitude) well beyond 6 GHz. Further improvement
173 of the model will require considering the parasitic inductance of the via and its skin effect.
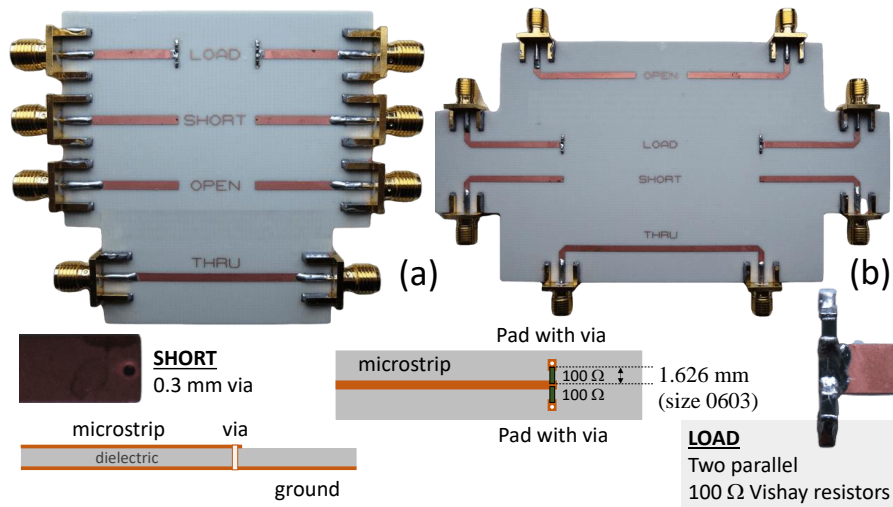

Fig. 2. Two types of PCB calibration cells used for the 3-term error correction model. (a)
straight cell; (b) dogbone cell.

178 LOAD is two 100 Ω Vishay RF resistors (case size 0603) soldered in parallel between
179 the microstrip and two via-grounded pads, thus having 50 Ω. Such configuration is used to
180 reduce the parasitic inductance associated with them. Up to 15 GHz, S_{11L} of such resistor
181 termination may be as low as −20 dB. Therefore, in the 3-term error correction model, we
182 assume that $S_{11L} = 0$ (linear magnitude). For RF resistors, Vishay provides LCR equivalent

183 circuits that could be used to model more accurately their S_{11L} as the terminations. However,

184 they still contain contact pads and vias for which the LCR parameters should also be considered.

185   Coplanar waveguide PCB cells could also be explored. Their calibration cells are more

186 convenient because SHORT and LOAD surface-mount terminations can be connected between

187 the microstrip and the adjacent ground planes on the same side. This plane is usually connected

188 to the main ground on the opposite side by a row of vias along the edge. Such arrangements

189 should minimise the parasitic parameters.

3. Multi-stage calibration for measuring the impedance of ferromagnetic wires on the PCB cells

192   The implemented calibration procedure, shown in Fig. 3, includes three stages: (i) full

193 2-port calibration of VNA and the cables attached to its ports using SOLT terminations (T

194 stands for THRU), (ii) de-embedding the microstrips using the 3-term error correction model,

195 and (iii) compensating the delay time along the sample using the unwrapped phase. The 2-port

196 SOLT calibration, also named TOSM in Rohde&Schwarz VNAs (M stands for MATCH), is

197 based on the 12-term error correction model which most fully describes the VNA error model

198 [43]. This type of calibration is implemented in all VNAs. All that is needed is a mechanical

199 calibration kit with SOLT coaxial standards and their analytical LCR models provided by the
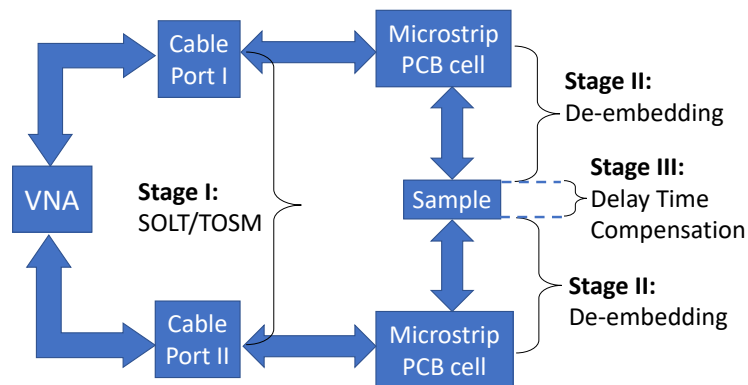
200 VNA manufacturer.

201

202 **Fig. 3.** Multi-stage calibration for impedance measurements.

203

204 *3.1. Stage I: SOLT calibration of VNA and cables*

205   Once SOLT calibration is completed and activated, it will be automatically applied to

206 all measurements in real-time. At the Stage I, the reference plane has already been extended to

207 the end of the cables. Now all S-parameters of microstrips can be recovered using the 3-term

208 error model shown in Fig. 4. The model operates with only three error parameters: E_{DF}

209 (directivity forward), E_{RF} (reflection tracking forward), and E_{SF} (source mismatch forward).

210 The actual reflection S_{11A} produced by a termination connected to the microstrip end is

211 entangled into S_{11M} measured from the coaxial connection soldered to the PCB:

212 $$S_{11M} = \frac{b_1}{a_1} = E_{DF} + \frac{E_{RF}S_{11A}}{1-S_{11A}E_{SF}} \tag{1},$$

213 where a_1 and b_1 represent input and output signals, respectively. By measuring three

214 reflections on the PCB calibration cell, where the microstrip is terminated with non-coaxial

215 SOL, it becomes possible to find E_{DF}, E_{RF}, and E_{SF}, and then recover all S-parameters of the

216 microstrip. Note that during these measurements the calibration cell is connected to the VNA

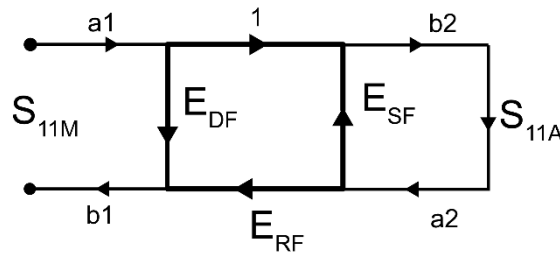217 and the cables which have been already calibrated at Stage 1.

218

219 **Fig. 4.** 3-term error correction model. $a_{1,2}$ and $b_{1,2}$ represent input and output signals,

220 respectively.

221

222 In Eq. (1), we have three unknowns E_{DF}, E_{RF}, and E_{SF} which can be found from S_{11M}

223 measured from the three known termination standards SHORT ($S_{11A} \rightarrow S_{11S}$), OPEN ($S_{11A} \rightarrow$

224 S_{11O}), and LOAD ($S_{11A} \rightarrow S_{11L}$):

225 $$\begin{cases} S_{11MS} = E_{DF} + \frac{E_{RF}S_{11S}}{1-S_{11S}E_{SF}} \\ S_{11MO} = E_{DF} + \frac{E_{RF}S_{11O}}{1-S_{11O}E_{SF}} \\ S_{11ML} = E_{DF} + \frac{E_{RF}S_{11L}}{1-S_{11L}E_{SF}} \end{cases} \tag{2}.$$

226 After getting rid of the denominators, the system of Eq. (2) becomes linear with respect to three

227 variables: $x = E_{DF}$, $y = E_{SF}$, and $z = (E_{RF} - E_{DF}E_{SF})$:

228 $$\begin{cases} E_{DF} + S_{11MS}S_{11S}E_{SF} + S_{11S}(E_{RF} - E_{DF}E_{SF}) = S_{11MS} \\ E_{DF} + S_{11MO}S_{11O}E_{SF} + S_{11O}(E_{RF} - E_{DF}E_{SF}) = S_{11MO} \\ E_{DF} + S_{11ML}S_{11L}E_{SF} + S_{11L}(E_{RF} - E_{DF}E_{SF}) = S_{11ML} \end{cases} \tag{3}.$$

229 For our terminations on the PCB calibration cells, we assumed $S_{11S} \equiv -1$, $S_{11O} \equiv 1$, and

230 $S_{11L} \equiv 0$ for the whole frequency range. If more accurate LCR models are available for the

231 terminations, the interpolated values can be used. Solving Eq. (3) numerically for each

232 frequency point within the sweep range set at SOLT of the VNA, all S-parameters of the

233 microstrip can be found for the whole frequency range: $S_{11} = x$, $S_{22} = y$, and $S_{21} = S_{12} =$

234 $\pm\sqrt{z + xy}$. The proper sign at the square root is chosen from the condition that the unwrapped

235 phase $\varphi = \pm\,arg\left(\sqrt{z + xy}\right)$ must have a negative slope. If the left and right microstrips are

236 not symmetrical, the measurements and calculations described above must be performed for

237 each microstrip.

3.2. Stage II: De-embedding microstrips

239 Modern VNAs allow embedding or de-embedding networks beyond the reference plane

240 by an already established calibration. The microstrips can be considered as the networks

241 connected beyond the reference plane at the cable ends. Thus, de-embedding them will extend

242 the reference plane to the sample interface. A diagram explaining the principles of 2-port de-

243 embedding is shown in Fig. 5. We follow the convention that S_{11} of a network faces the port

244 to which it is connected.

$$\begin{pmatrix} b_2 \\ a_2 \end{pmatrix} = \widehat{\mathbf{P}}_1 \begin{pmatrix} a_1 \\ b_1 \end{pmatrix} \qquad \begin{pmatrix} b_4 \\ a_4 \end{pmatrix} = \widehat{\mathbf{P}}_A \begin{pmatrix} a_3 \\ b_3 \end{pmatrix} \qquad \begin{pmatrix} b_6 \\ a_6 \end{pmatrix} = \widehat{\mathbf{P}}_2 \begin{pmatrix} a_5 \\ b_5 \end{pmatrix}$$
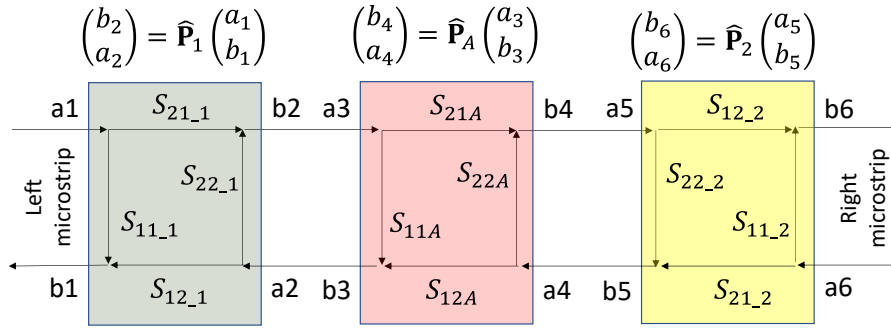
Fig. 5. Principles of 2-port de-embedding.

248 S-matrices do not allow performing calculations with cascaded networks, *i.e.* the

249 product of the S-matrices of two cascaded networks is not equal to the S-matrix of the combined

250 network. To carry out matrix calculations with cascading networks, we must operate with the

251 propagation P-matrices, which can be introduced as follows:

252 $$\begin{pmatrix} b_2 \\ a_2 \end{pmatrix} = \widehat{\mathbf{P}} \begin{pmatrix} a_1 \\ b_1 \end{pmatrix} \tag{4}.$$

253 It relates the input and output at the left with the input and output at the right. P-parameters can

254 be expressed through S-parameters:

255 $$\widehat{\mathbf{P}} = \begin{pmatrix} \frac{S_{12}S_{21}-S_{22}S_{11}}{S_{12}} & \frac{S_{22}}{S_{12}} \\ -\frac{S_{11}}{S_{12}} & \frac{1}{S_{12}} \end{pmatrix} = \frac{1}{S_{12}}\begin{pmatrix} S_{12}S_{21} - S_{22}S_{11} & S_{22} \\ -S_{11} & 1 \end{pmatrix} \tag{5}.$$

257 In turn, S-parameters can be expressed through P-parameters:

258 $$\hat{\mathbf{S}} = \begin{pmatrix} -\frac{P_{21}}{P_{22}} & \frac{1}{P_{22}} \\ P_{11} - \frac{P_{12}P_{21}}{P_{22}} & \frac{P_{12}}{P_{22}} \end{pmatrix} \tag{6}.$$

259 The sample stacked between two microstrips constitutes a combined network with the
260 propagation matrix $\hat{\mathbf{P}}_2\hat{\mathbf{P}}_A\hat{\mathbf{P}}_1$ (see Fig. 5):

261 $$\begin{pmatrix} b_6 \\ a_6 \end{pmatrix} = \hat{\mathbf{P}}_2\hat{\mathbf{P}}_A\hat{\mathbf{P}}_1 \begin{pmatrix} a_1 \\ b_1 \end{pmatrix} = \hat{\mathbf{P}}_M \begin{pmatrix} a_1 \\ b_1 \end{pmatrix} \tag{7}.$$

262 Here, $\hat{\mathbf{P}}_1$ and $\hat{\mathbf{P}}_2$ are the known propagation matrices of the left and right microstrips
263 respectively, obtained using the PCB calibration cell, 3-term model, and Eq. (5). $\hat{\mathbf{P}}_A$ is the
264 unknown propagation matrix of the sample. On the other hand, $\hat{\mathbf{P}}_M = \hat{\mathbf{P}}_2\hat{\mathbf{P}}_A\hat{\mathbf{P}}_1$ of the combined
265 network can be obtained by measuring its S-parameters and using Eq. (5). Therefore, $\hat{\mathbf{P}}_A =$
266 $\hat{\mathbf{P}}_2^{-1}\hat{\mathbf{P}}_M\hat{\mathbf{P}}_1^{-1}$, where all three matrices at the right are known. Then, $\hat{\mathbf{P}}_A$ can be recalculated to $\hat{\mathbf{S}}_A$
267 using Eq. (6). Note that for the 2-port de-embedding, the whole matrix $\hat{\mathbf{S}}_M$ of the combined
268 network must be measured. Whereas, for the 1-port de-embedding, S_{11A} can be recovered from
269 S_{11M} (see Eq. (1)):

270 $$S_{11A} = \frac{S_{11M}-E_{DF}}{E_{RF}+E_{SF}(S_{11M}-E_{DF})} \tag{8}.$$

271   In our measurement setup, we use Rohde&Schwarz (R&S) ZNB20 2-port VNA, 100
272 kHz – 20 GHz. In this VNA, the de-embedding can be performed automatically after uploading
273 the S2P Touchstone text file (.s2p) for each network. If the networks are symmetrical as in our
274 case, the same file can be uploaded for both ports. The S2P file includes the header # Hz S RI
275 R 50 and consists of nine tab-delimited columns: frequency [Hz], $\text{Re}[S_{11}]$, $\text{Im}[S_{11}]$, $\text{Re}[S_{21}]$,
276 $\text{Im}[S_{21}]$, $\text{Re}[S_{12}]$, $\text{Im}[S_{12}]$, $\text{Re}[S_{22}]$, $\text{Im}[S_{22}]$. We have developed a Python program code,
277 available at a public repository on GitHub [44], which creates S2P files of the microstrips from
278 $S_{11/22MSOL}$ (see Eq. (3)) measured from the PCB calibration cell. The surface-mount
279 terminations can be considered ideal or have dispersion behaviour saved in $S_{11/22SOL}$. Also, the
280 algorithm can perform the 1-port or 2-port de-embedding if this option is not available in an
281 old VNA model. Further details can be found in the manual on GitHub.

282

After activating SOLT calibration and de-embedding (Stages I and II), S_{11A} and S_{21A} of the sample can be correctly measured. For the 1-port and 2-port measurements, the sample impedance is calculated as follows:

$$Z_A = 50 \times \frac{1+S_{11A}}{1-S_{11A}} [\Omega] \qquad (9),$$

$$Z_A = 100 \times \frac{(1-S_{21A})}{S_{21A}} [\Omega] \qquad (10).$$

However, these equations assume that the sample is lumped, *i.e.* it has zero electrical length, or at least much shorter than the wavelength. This condition is not met in our case. A piece of wire above a continuous ground is a waveguide structure resulting in a phase incursion. Compensating for this phase incursion constitutes Stage III in our calibration procedure (Fig. 3), which will be explained next.

3.3. Stage III: Phase unwrapping and delay time compensation along the wire sample

Our measurement cells are 2-port. Typical phase dispersions of S_{21A} measured in ferromagnetic wire samples on the straight and dogbone PCB cells are shown in Figs. 6(a, b), respectively. Piecewise negative phase slopes separated by device induced jumps (phase can be measured only within $[-\pi, \pi]$) are caused by the delay time along the wire. They may be distorted due to parasitic resonances and deterioration in the de-embedding accuracy at higher GHz frequencies. For any analysis and further processing, the phase must be free from 2π jumps and returned to a continuous form with a negative slope. By fitting this slope in a certain frequency range with a straight trend line $\varphi(f) = af + b$, where f is the frequency, the delay time can be calculated as $\Delta t = |a|/(2\pi)$. Although phase unwrapping is available in modern VNAs, performing it directly on the device may be difficult. When allocating a certain frequency interval for unwrapping, VNA may show point spikes caused by numerical uncertainties during de-embedding. These spikes will not allow the phase to be unwrapped correctly. Therefore, it is desirable to save the raw phase dispersion over the entire range in a csv/text file, truncate the frequency interval as proposed in Fig. 6, and then unwrap the phase numerically. The corresponding Python algorithm is available at our public GitHub repository in the folder Delay time [44]. To calculate the impedance using Eq. (10), S_{21A} must be replaced by the corrected $\tilde{S}_{21A}(\omega) = S_{21A}(\omega) \times \exp{(i\omega\Delta t)}$. This completes the Stage III of calibration.
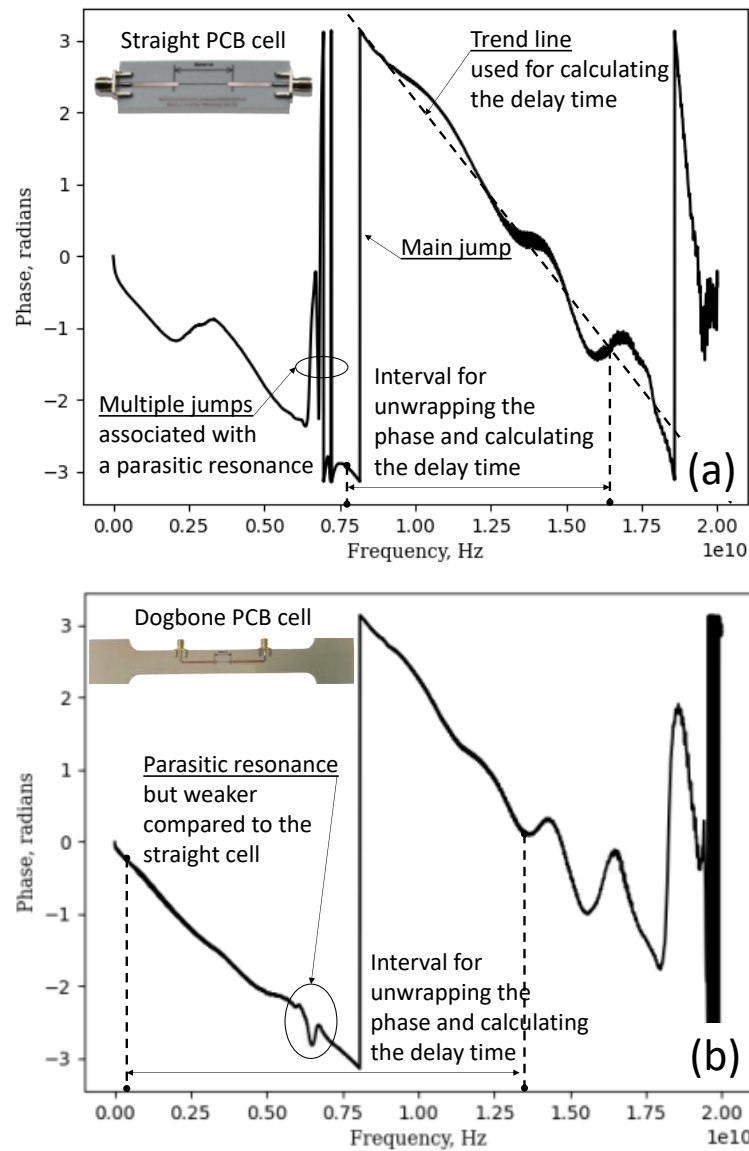
Fig. 6. Phase dispersions of S_{21A} measured in ferromagnetic wire samples on the straight (a) and dogbone (b) PCB cells.

3.4. Impedance measurement setup

To measure the impedance, we designed the setup shown in Fig. 7. It includes three programmable R&S devices: ZNB20 VNA (2-port, 100 kHz – 20 GHz), Function Generator HMF2550, and HMC 8012 Digital Multimeter (DMM). The only analog device is Accel Instruments Waveform Amplifier TS250-2 used for feeding a Helmholtz coil. All devices are mounted on a trolley, which allows the setup to be parked next to various installations, such as a stress machine or a bench with the coil. Impedance measurements require three programmable devices to operate in sync according to the block diagram shown in Fig. 8. The device control was implemented in LabVIEW 2015 through NI VISA driver. SOLT calibration

325   (Stage I) and de-embedding (Stage II) are already activated on VNA before starting

326   measurements. The program iterates the DC offset voltage at the output of the function

327   generator from its minimum $-V_g$ to maximum $+V_g$ with the specified number of points N. The

328   DC offset output is applied to the power amplifier to feed the Helmholtz coil. After applying a

329   voltage, the operation is paused for the time duration of $20 \times L/R$, where L and R are the coil

330   inductance and resistance, to achieve the saturation of the coil current. The VNA sweep is then

331   activated to measure $S_{21/11}$ at discrete frequency points (N_f). During this sweep, the field is

332   kept constant. The actual voltage applied to the coil after the power amplification is measured

333   by the DMM. Its value is passed to the program to be recalculated into the field using the coil

334   calibration coefficient (Oe/V). The real and imaginary parts of the measured S-parameter are

335   transferred as an array to the PC, where they are corrected to compensate for the sample delay

336   time (Stage III), and then converted into impedance using Eq. (9) or (10). The measurement

337   process is repeated in a loop for the next field point. To reproduce possible magnetic hysteresis

338   properties, the DC offset is iterated in both directions: from negative to positive values (loop

339   forward) and then in the inverse direction (loopback). Stress and temperature measurements

340   are currently not integrated into the control program. These parameters are changed manually
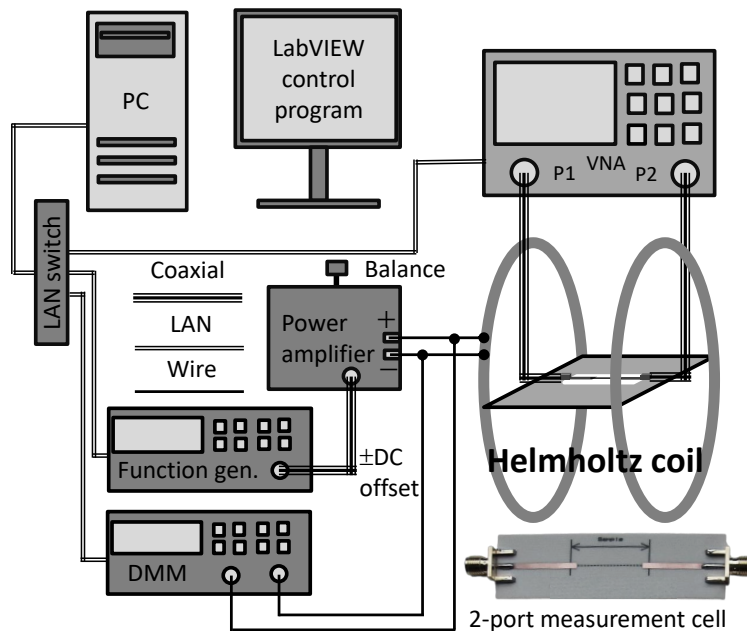
341   after a loop over the field points is completed.

342

343   **Fig. 7.** Automated setup for measuring the field dependence of the impedance.
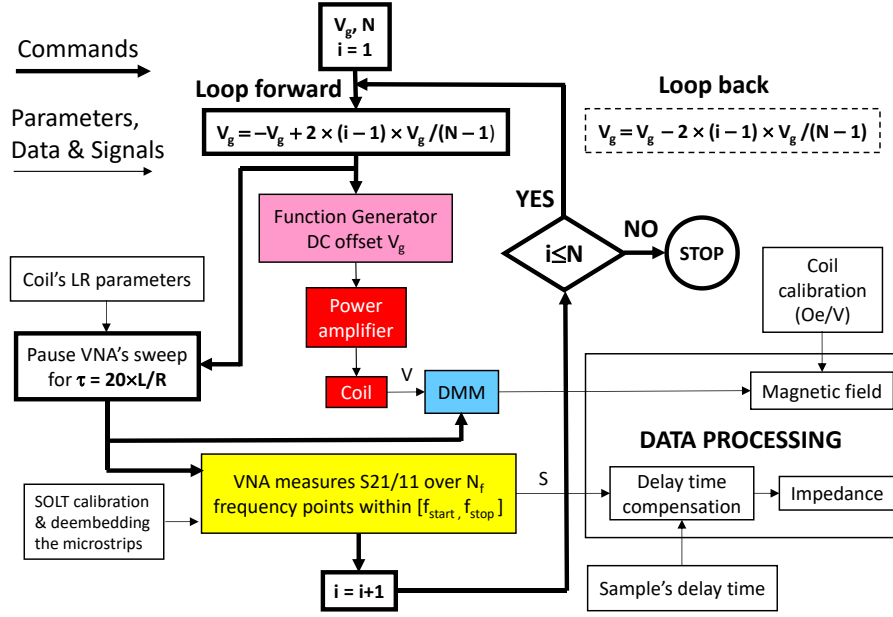
344

Fig. 8. Block diagram of the LabVIEW control program that synchronizes the operation of three R&S devices for measuring the field dependence of the impedance.

4. Broadband impedance measurement under in-situ magnetic field and stress

As an illustration of the proposed measurement technique, Fig. 9 shows a broadband dispersion of the impedance in a glass-coated ferromagnetic wire. The continuous wire reel, kindly provided by MFTI Ltd (Republic of Moldova), was fabricated by the Taylor-Ulitovskiy method [17] from a Co-based alloy of the composition $Fe_4Co_{68.7}Ni_1B_{13}Si_{11}Mo_{2.3}$ (wt.%) The total wire diameter, including the glass shell, was 23.2 μm with a metal core of 19.1 μm. A piece of wire 20 mm long was fixed on a dogbone PCB cell. The impedance was recalculated from $\tilde{S}_{21A}$ using Eq. (10) over the frequency range $1\,\text{MHz} - 15\,\text{GHz}$ in the presence of longitudinal DC bias fields. As will be shown in the next section, the uncertainty in determining the delay time along the sample used for the correction of S_{21A} (Stage III) does not exceed ± 3 ps or less than ± 0.5 mm in terms of the sample length.

In ferromagnetic wires, the magnetic AC permeability arises as a result of the magnetization precession induced by the circular magnetic field when passing a high-frequency current. Conductivity and effective AC permeability together determine the skin-depth for the high-frequency current. In Co-based glass-coated wires having negative magnetostriction, the equilibrium magnetisation has a circular direction which can be deflected by applying a moderate longitudinal DC magnetic field. This leads to a field dependence of the AC permeability and, as a result, the impedance [1]. The most noticeable effect in this type of wire is a broad FMR, which gradually develops when a longitudinal magnetic field is applied, as

shown in Fig. 9. The curves after 2.5 GHz demonstrate many irregular disturbing wave peaks. As shown in the next section, the wave peaks in the vicinity of 6-7 GHz and then 14 GHz are unambiguously identified as parasitic LC resonance on the PCB cell and are well described by the second-order terms in the dispersion equation. Other wave peaks of smaller amplitudes should be attributed to the same reason but will require a larger number of resonance terms to be fitted. It should also not be discounted that large amplitude changes mask measurement uncertainties that begin to show up in quieter intervals. The impedance amplitude reaches its maximum value around 1 GHz when the magnetisation is saturated along the wire axis. As FMR is not the subject of study in this work, we mention it only because in its vicinity the impedance will demonstrate maximum sensitivity to external stimuli, which is important for applications where tunable scattering properties are required.

In Fig. 10, the stress dependence of the impedance was measured in the vicinity of FMR at 900 MHz at different longitudinal bias fields. The dogbone PCB cell was stretched between the grippers of a desktop Instron machine. The strain was measured by an optical camera method [39]. On one hand, stress sensitivity requires the magnetisation to be deflected from the circular direction. Without external magnetic field, the stress sensitivity of impedance is negligible (yellow trace). On the other hand, magnetisation saturated along the wire axis by a strong longitudinal field will require a larger tensile stress to rotate it back into the circular direction. This tension may be outside the elastic regime. Thus, there should be an optimal longitudinal external field that provides the largest stress sensitivity of the impedance within the elastic regime. For the sample in Fig. 10, the optimal bias field which produces largest stress sensitivity of impedance is about 3.6 Oe. The Earth's magnetic field will make the curves flatter or steeper, depending on the geometrical sum with the external bias field. It will also shift them as a whole along the impedance axis. The magnitude of both effects will decrease as the bias field increases, which magnetically saturates the wire. We estimated the maximum vertical shift of the curve caused by the Earth's field at the optimal bias field from the preceding (2.7 Oe) and following (4.46 Oe) curves. It is about ± 20 Ω.
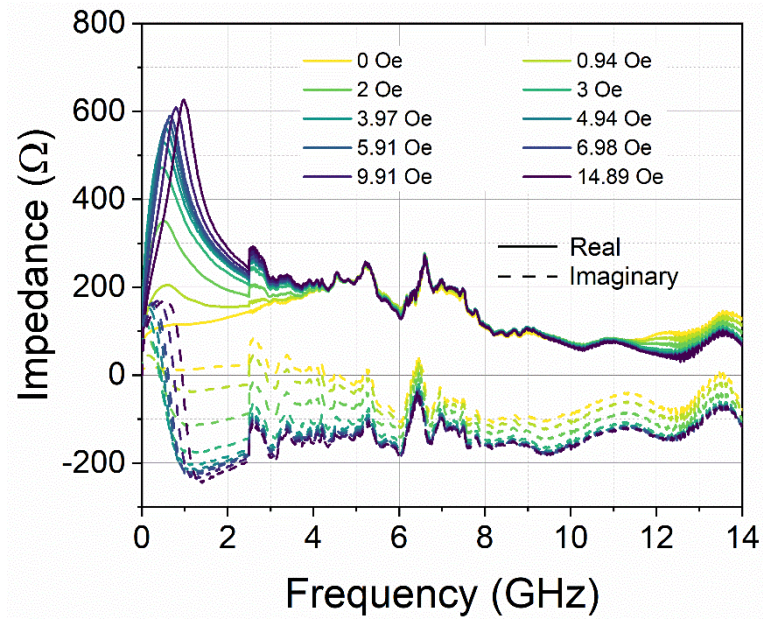
Fig. 9. Broadband dispersion of the impedance recalculated from the corrected $\tilde{S}_{21A}$ at different longitudinal bias fields. Three-stage calibration has been applied.
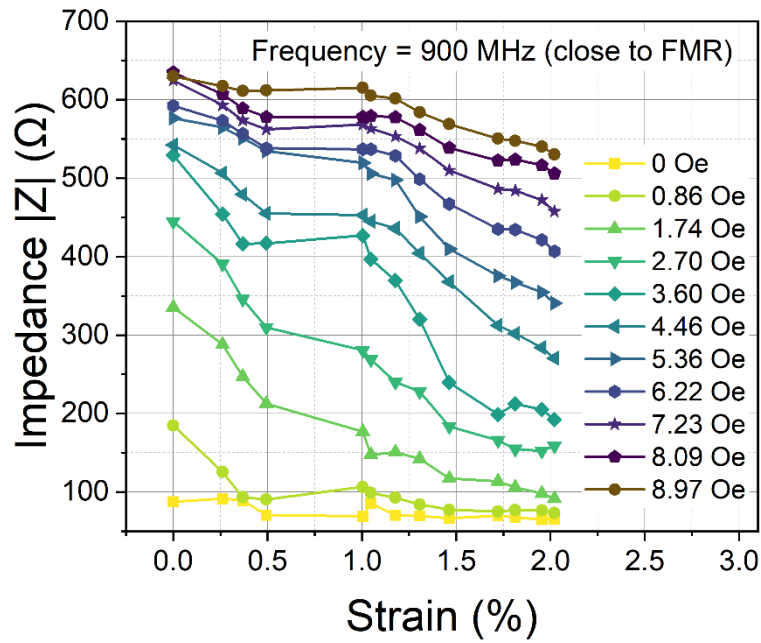

Fig. 10. Stress dependence of the wire impedance measured at a fixed frequency in the vicinity of FMR at different longitudinal bias fields.

5. Surface impedance of ferromagnetic wires as a boundary condition in scattering simulations

In the cm-wave range, the skin depth is comparable to the micron radius of the wire. The entire volume of the wire with its conductive and magnetic properties will be involved in the formation of the scattered electromagnetic field. Widely used models [37,38] cannot accurately reproduce MI properties in the frequency range of interest for scattering applications (transition from MHz to GHz). This prompts us to develop a method for measuring surface impedance as a boundary condition for scattering problems. The definition of the surface impedance tensor $\hat{\varsigma}$ given in CST coincides with that in Ref. [45]:

$$\bar{\mathbf{E}}_t = \hat{\varsigma}(\bar{\mathbf{H}}_t \times \mathbf{n}) \tag{11},$$

where the tangent vector of the total electric field $\bar{\mathbf{E}}_t$ at the wire surface is expressed through the vector product of the unit normal vector $\mathbf{n}$ directed inside the conductor and the tangent magnetic field $\bar{\mathbf{H}}_t$ at the wire surface. In the cylindrical coordinate system (x, φ, r) associated with the wire, the impedance boundary condition can be written in the coordinate form:

$$\begin{cases} \bar{E}_x = \varsigma_{xx}\bar{H}_\varphi - \varsigma_{x\varphi}\bar{H}_x \\ \bar{E}_\varphi = \varsigma_{\varphi x}\bar{H}_\varphi - \varsigma_{\varphi\varphi}\bar{H}_x \end{cases} \tag{12}.$$

In a nonmagnetic conductor, $\varsigma_{x\phi/\phi x} \equiv 0$. The presence of the off-diagonal components is a distinctive feature of ferromagnetic samples with a certain type of magnetic anisotropy. The use of these components for sensor applications in the MHz range has already been explored previously [46]. A thin wire only allows one wave polarization that is essential for the formation of a scattered field: with an electric vector along the wire. Therefore, $\varsigma_{x\varphi}\bar{H}_x$ in the first equation in Eq. (12) can be neglected. The second equation in Eq. (12) defines the induced circular current, which will introduce a negligibly smaller radiation additive compared to the longitudinal induced current. Therefore, this equation can be neglected. Only one equation remains essential for scattering problems: $\bar{E}_x = \varsigma_{xx}\bar{H}_\varphi$.

CST allows experimental impedance boundary conditions for solving external electrodynamic problems. The impedance can be provided in a tabular form: frequency, real part, and imaginary part. These values are then interpolated using a predefined template that includes first and second-order resonant terms. When calculating the wire impedance Z from the corrected $\tilde{S}_{21A}$, the delay time along the sample is fully compensated, thus reducing its effective electrical length to zero. The total current I along such an ideal impedance element does not have a longitudinal distribution, as well as $\bar{E}_x$. The circular magnetic field on the surface of the wire is $\bar{H}_\varphi^{SI} = I/2\pi a = V/2\pi aZ = l\bar{E}_x/2\pi aZ$ (SI units) or $\bar{H}_\varphi^{cgs} = 2l/ac =$

435 $2V/acZ = 2l\bar{E}_x/acZ$ (cgs units). Here, a and l are the wire radius and length respectively,

436 and $c = 2.99792458 \times 10^{10}$ cm/s is the speed of light (cgs). Using these equations, for the

437 longitudinal surface impedance $\varsigma_{xx} = \bar{E}_x/\bar{H}_\varphi$, we obtain:

438 $\varsigma_{xx}^{SI}[\Omega/sq] = Z[\Omega] \times \frac{2\pi a}{l}$ (13),

439 $\varsigma_{xx}^{cgs}[(s/cm)/sq] = Z[\Omega] \times \frac{10^9 a}{2lc}$ (14).

440 In Eq. (14), the normalization factor is chosen so that the impedance is measured in Ohms. The

441 notations Ω/sq and $(s/cm)/sq$ adopted here refers to the surface (sq). The wire parameters a

442 and l can be measured in any units because they enter the equation as a ratio.

443   The CST Studio Suite (release version 2022.04) offers a multi-resonance physical

444 model along with numerical optimization to fit the experimental surface impedance dispersion:

445 $\varsigma(\omega) = \varsigma_\infty + i\omega L + \sum_{n=1}^{N} \frac{\beta_{0,n}}{\alpha_{0,n}+i\omega} + \sum_{n=1}^{M} \frac{\gamma_{0,n}+i\omega\gamma_{1,n}}{\delta_{0,n}+i\omega\delta_{1,n}-\omega^2}$ (15).

446 The fitting parameters have the following physical interpretations. The 1st order resonance

447 terms ($n = \overline{1,N}$): frequency of the pole $f_{p1,n} = \alpha_{0,n}/2\pi$ [Hz], static gain contribution $g_{1,n} =$

448 $\beta_{0,n}/\alpha_{0,n}$ [Ω/sq]. The 2nd order resonance terms ($n = \overline{1,M}$): resonance frequency $f_{p2,n} =$

449 $\sqrt{\delta_{0,n}}/2\pi$ [Hz], quality factor $Q_{2,n} = \sqrt{\delta_{0,n}}/\delta_{1,n}$, frequency of the zero $f_{z2,n} = \gamma_{0,n}/2\pi\gamma_{1,n}$

450 [Hz], static gain contribution $g_{2,n} = \gamma_{0,n}/\delta_{0,n}$ [Ω/sq]. The maximum number of resonant

451 terms used for a fitting cannot exceed 10, including the order of the poles. For example, two

452 resonances of 1st order and four resonances of 2nd order.

453   Fig. 11 illustrates the principles of impedance fitting used in CST. The dispersion curves

454 for the real and imaginary parts of ς_{xx} (Exp_real/imag) in the presence of an external

455 longitudinal bias field (3.97 Oe) were fitted with $\varsigma_\infty = 0.00647476$ Ω/sq, $L = 1.07214 \times$

456 10^{-12} H, two resonance terms of 1st order, and three resonance terms of 2nd order. The physical

457 parameters for the resonance terms are shown in Table 1. The total fitting order 8 was set in

458 the program interface, and the choice of resonant terms between the 1st and 2nd orders was made

459 automatically by the CST optimization algorithm. The fitting was able to identify and

460 accurately describe the parasitic LC resonances at $6-7$ GHz ($f_{p2,2}$ and $f_{p2,3}$) and 14 GHz

461 ($f_{p2,1}$), caused by the measurement cell. A larger number of terms in Eq. (15) could make it

462 possible to approximate a larger number of wave peaks observed after 2.5 GHz. However, the

463 main purpose of such a fitting is, on the contrary, to cut off effects that are not related to the

464 conductive and magnetic properties of the sample. The 1st order model is responsible for

465 magnetic resonance properties, revealing two poles with $f_{p1,1} \approx 200$ MHz and $f_{p1,2} \approx 1$ GHz.

466 The sum of these two terms decays as $1/\omega$ at $\omega \to \infty$ and proportional to ω at $\omega \to 0$ due to

467 $g_{1,1}$ and $g_{1,2}$ having close absolute values and opposite signs. The gains $g_{2,n}$ $(n = \overline{1,3})$ are

468 significantly smaller, and hence the 2nd order model contributes much less within the frequency
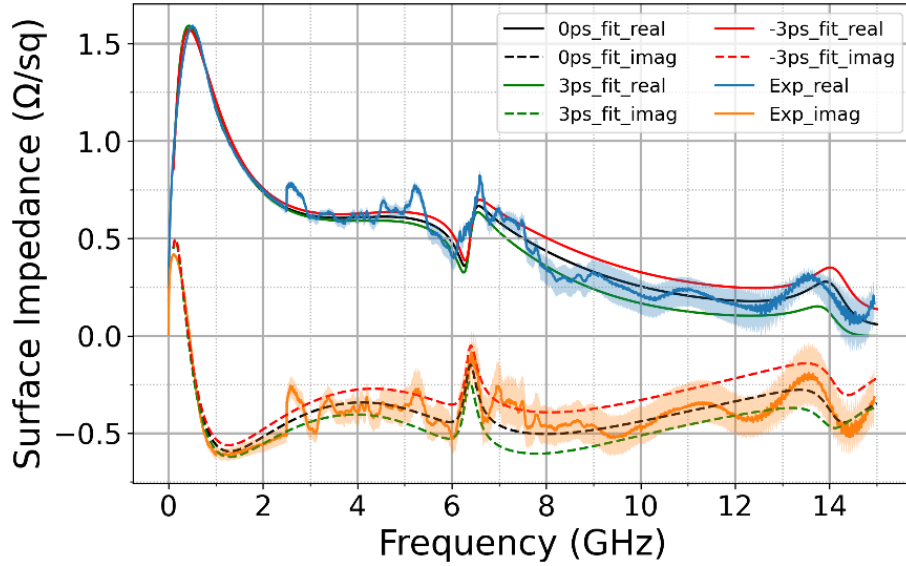
469 range $[f_{p1,1}, f_{p1,2}]$.

470

Fig. 11. The dispersion curves for the real and imaginary parts of ς_{xx} in the presence of an external longitudinal bias field 3.97 Oe fitted with the model template in Eq. (15). The impedance tolerance caused by the uncertainty of the delay time is shown.

474

Table 1. Physical parameters of the 1st and 2nd order resonance models used to fit the impedance dispersion in Fig. 11.

N	1	2	3
f_{p1} [GHz]	0.200253	1.03141	
g_1 [Ω/sq]	−1.54142	1.76759	
f_{p2} [GHz]	14.1188	6.36786	6.76186
Q_2	14.6469	20.9207	0.965668
f_{z2} [GHz]	12.8863	15.2074	4.53192
g_2 [Ω/sq]	0.00964765	−0.014956	0.340934

477

478 When recalculating the corrected $\tilde{S}_{21A}$ into the impedance, even a slight error in the

479 delay time (determined from the unwrapped phase), may violate physical conditions imposed

480 on the impedance dispersion. Thus, further adjustment is needed to ensure that the real part of

481 the impedance remains positive and tends to zero at higher GHz frequencies. As for the

482 imaginary part of the impedance, it is not physically forbidden to go into the positive region.

483 However, if a premature transition is exhibited caused by an error in the delay time, this will

cause the real part to grow again, which will be noticeable. Ignoring these physical conditions makes impedance measurements practically useless [30]. An adjustment algorithm for the delay time is used here and available at GitHub repository in the folder Impedance dispersion [44]. As the frequency increases, both the real and imaginary curves are asymptotically approaching the horizontal axis, thereby reducing the tolerated uncertainty in the delay time. In Fig. 11, the experimental solid curves of the real and imaginary parts of the impedance were reconstructed from $\tilde{S}_{21A}$ with the calculated and slightly adjusted delay time. These reference curves (0 ps delay time uncertainty) were fitted (0ps_fit_real/imag) with the CST model template in Eq. (15). The shadows accompanying the reference curves correspond to the impedance reconstructed from $\tilde{S}_{21A}$ with the delay time uncertainty limits ± 3 ps, which, however, does not violate the physical conditions, at least up to 15 GHz. The curves for these uncertainty limits were also fitted with the model template (± 3ps_fit_real/imag). It can be seen that the fitting curves for 0 ps are better centred with respect to their parent experimental curves. Thus, fitting with the theoretical model can serve as an additional criterion for minimizing the error in the delay time. Our PCB cells allow de-embedding up to 15 GHz. For this frequency range, the delay time uncertainty cannot exceed ± 3 ps. This corresponds to ± 0.5 mm uncertainty in the sample length, given that the speed factor of wave propagation over PCB is ~ 0.6. Compared with our measurements, the measurement proposed before was limited to 3 GHz [31], which do not allow any conclusions to be drawn about the accuracy of the phase compensation along the sample. Also, there was no analysis carried out on the correspondence of measurements to impedance models that would guarantee the fulfilment of the Kramers-Kronig relations.

Correct calculation of the impedance from S-parameters makes it possible to reveal important effects associated with the magnetic structure. It has been shown that for wires with a circular anisotropy, the impedance dependence on the external longitudinal field cannot be described by existing models in the MHz to GHz transition [39,47]. A typical impedance transformation scenario observed in the experiment is shown in Fig. 12. The projection of the Earth's magnetic field on the wire axis will shift the magneto-impedance characteristics along the field axis, but the shape of the curves will not be affected. Starting around 700 MHz, when the change in impedance with field reaches its maximum, there is a bending point in the curve producing a double slope (800 MHz). As the frequency increases, the bending point remains fixed relative to the field axis, while the maximum shifts toward higher fields. The impedance value at the bending point is gradually decreasing. For frequencies above 5 GHz, the maxima

517 shift so far that the impedance curve looks like a horizontal line. In theory, however, such
518 phenomena are not predicted. There is a gradual rise in the wings of the curve after the maxima
519 with increasing frequency, while these maxima remain fixed relative to the field axis. The
520 discrepancy between theory and experiment occurs in the MHz to GHz frequency range which
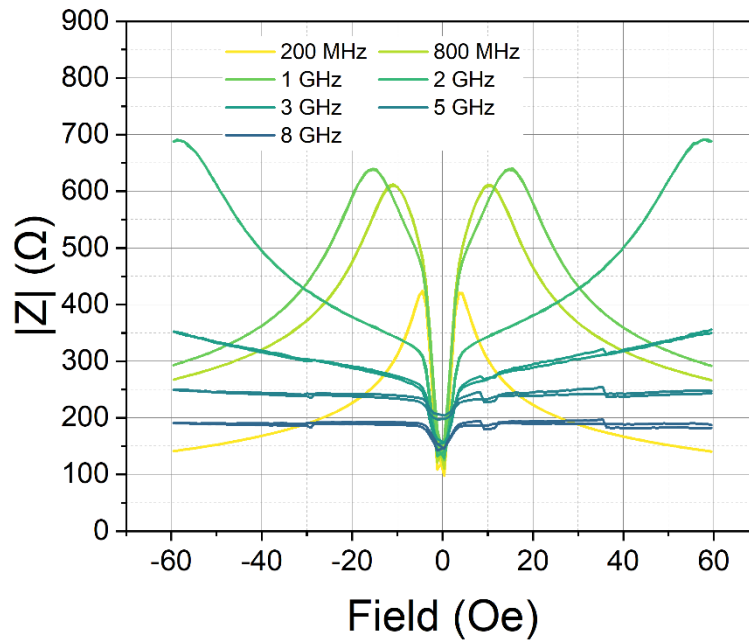521 is pivotal for scattering applications.

522

523 **Fig. 12.** The magneto-impedance transformation scenario when transitioning from the MHz
524 to GHz ranges.

525

526   The question of how to construct a rigorous scattering theory for wire inclusions
527 remains open. The solution to the internal problem is impossible due to the complex magnetic
528 domain structure. Further progress will be made through the development of hybrid methods
529 in which the external scattering problem is solved numerically along with experimental
530 impedance boundary conditions. The single-particle scattering problem is the first step in this
531 direction. The approach using the antenna integro-differential equation for the wire current
532 does not require the mesh as in more universal finite-element methods [40]. However, the
533 solution of many such equations interlocking through a complex operator of electromagnetic
534 interaction between inclusions would be numerically costly. It would also be worthwhile to
535 explore the extent to which CST can be used for such simulations. In a single-particle problem,
536 we calculated the distribution of the surface circular magnetic field $\bar{H}_\varphi$ along a wire 50 mm
537 long and 19.1 μm in diameter induced by a plane wave (Fig. 13). The 1.5 GHz wave was
538 linearly polarized with an electric field (1 V/m) along the wire. The experimental surface

539　　impedance was used as the boundary condition. The field $\bar{H}_\varphi$ is a measure of the total effective

540　　current $I = 2\pi a \bar{H}_\varphi$ induced by the wave, which takes zero values at the ends of the wire

541　　fulfilling the boundary conditions. A sufficiently dense mesh is required to reduce the

542　　simulation error on the surface of the wire. We tried using "the cells per max model box edge"

543　　(simulation option in CST) equals 10 or 100. The number 10 provides a non-physical

544　　periodical angular dependence of $\bar{H}_\varphi$ on the wire surface, while it should be constant. The

545　　simulations shown in Fig. 13 used 100 cells resulting in a much smaller ripple of $\bar{H}_\varphi$ over the

546　　azimuthal angle φ. The field values were obtained by averaging $\bar{H}_\varphi$ over φ for each

547　　longitudinal position with a 5 mm step. The simulation has been done on a DELL XPS 8930

548　　computer (i7-9700 CPU@3.00 GHz, RAM 32 GB, Windows 10 Pro, 64-bit operating system).

549　　The computation time ranges from seconds to a few minutes depending on the mesh numbers.

550　　Using a detailed mesh to model such a thin wire compared to its length and wavelength does

551　　not look quite reasonable. This issue should be further addressed.
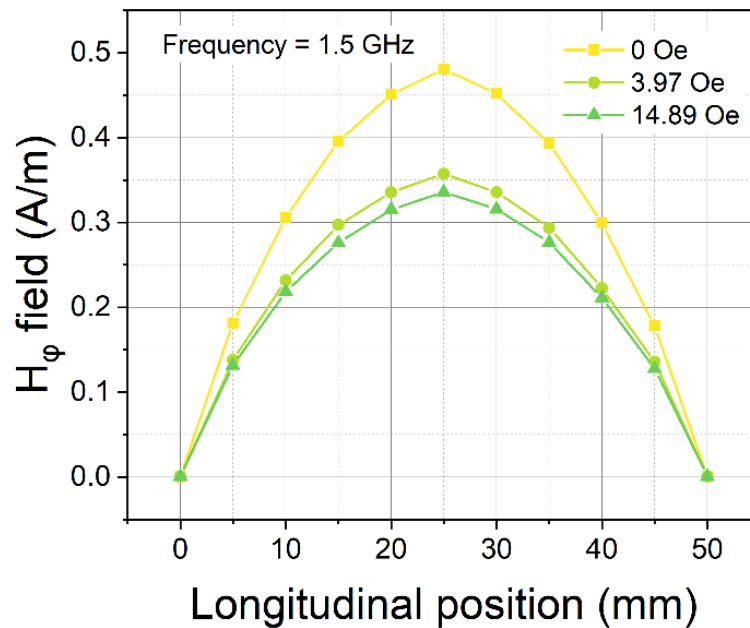

Fig. 13. Distribution of the surface circular magnetic field along a 50 mm wire dipole induced by the plane wave with the electrical field along the wire. The experimental surface impedance was used as the boundary condition at three values of the bias field.

557 As the computation power increases, the preferences of researchers will certainly shift
558 toward universal solvers. Therefore, we see broad prospects for using CST for modelling
559 electromagnetic properties of composite structures with wire inclusions. The hybrid approach
560 removes one of the significant obstacles which is finding the solution of the complicated
561 internal problem. The rest is purely an electrodynamic task that dispenses with complex
562 material properties.

563

6. Conclusion

565 We have developed a broadband measurement technique for the surface impedance of
566 ferromagnetic wires up to 15 GHz. It includes a three-stage calibration procedure: SOLT
567 calibration of VNA and coaxial cables, de-embedding of microstrips, and compensation of the
568 delay time (phase incursion) along the wire sample. The impedance is measured on PCB cells
569 to allow external magnetic field, tensile stress, and heating stimuli. De-embedding of
570 microstrips is implemented using the specially designed calibration PCB cells with the surface
571 mount SOL terminations. By measuring three reflection coefficients on the calibration cells
572 and using the 3-term model, the S-parameters of the microstrips can be determined.
573 Compensation of the delay time along the sample was implemented using the phase
574 unwrapping technique. The ability to carry out de-embedding up to 15 GHz made it possible
575 to reduce the uncertainty in determining the delay time to $\pm$ 3 ps. The accuracy of the
576 impedance measurements has been verified by fitting the dispersion model provided by the
577 CST Studio Suite, which ensures meeting the Kramers-Kronig relations. Use of experimental
578 impedance boundary conditions for scattering problems was tested in CST to calculate the
579 current distribution in a wire dipole induced by an electromagnetic wave. The hybrid approach
580 combining experimental material parameters and electrodynamic simulations provide solid
581 ground for designing the microwave response of wire-filled composite materials.

References

[1]   L.V. Panina, K. Mohri, Magneto-impedance effect in amorphous wires, Appl. Phys. Lett. 65 (1994) 1189–1191. doi:10.1063/1.112104.

[2]   D. Ménard, M. Britel, P. Ciureanu, A. Yelon, V.P. Paramonov, A.S. Antonov, P. Rudkowski, J.O. Ström-Olsen, High frequency impedance spectra of soft amorphous fibers, J. Appl. Phys. 81 (1997) 4032–4034. doi:10.1063/1.364927.

[3]   M. Dominguez, J.M. Garcia-Beneytez, M. Vazquez, S.E. Lofland, S.M. Bhagat, Microwave response of amorphous microwires: Magnetoimpedance and ferromagnetic resonance, J. Magn. Magn. Mater. 249 (2002) 117–121. doi:10.1016/S0304-8853(02)00517-6.

[4]   A. Zhukov, L. Gonzalez-Legarreta, M. Ipatov, P. Corte-Leon, J.M. Blanco, V. Zhukova, Giant magnetoimpedance effect at GHz frequencies in amorphous microwires, AIP Adv. 9 (2019). doi:10.1063/1.5129891.

[5]   J. Alam, M. Nematov, N. Yudanov, S. Podgornaya, L.V. Panina, High-frequency magnetoimpedance (MI) and stress-MI in amorphous microwires with different anisotropies, Nanomaterials. 11 (2021). doi:10.3390/nano11051208.

[6]   Z. Zhu, M. Peng, Y. Wang, F.X. Qin, Ultra-large giant magnetoimpedance effect by a 2D square spiral amorphous microwire, J. Magn. Magn. Mater. 550 (2022) 169090. doi:10.1016/j.jmmm.2022.169090.

[7]   M. Knobel, J. Schoenmaker, J.P. Sinnecker, R.S. Turtelli, R. Grössinger, W. Hofstetter, H. Sassik, Giant magneto-impedance in nanocrystalline $Fe_{73.5}Cu_1Nb_3Si_{13.5}B_9$ and $Fe_{86}Zr_7B_6Cu_1$ ribbons, Mater. Sci. Eng. A. 226–228 (1997) 546–549. doi:10.1016/s0921-5093(96)10682-1.

[8]   D. Stanescu, P. Xavier, J. Richard, C. Dubourdieu, Evidence of the magnetoimpedance effect up to microwave frequencies in polycrystalline La0.7Sr0.3MnO3 films, J. Appl. Phys. 99 (2006). doi:10.1063/1.2189202.

[9]   K. Agra, T.J.A. Mori, L.S. Dorneles, V.M. Escobar, U.C. Silva, C. Chesman, F. Bohn, M.A. Corrêa, Dynamic magnetic behavior in non-magnetostrictive multilayered films grown on glass and flexible substrates, J. Magn. Magn. Mater. 355 (2014) 136–141. doi:10.1016/j.jmmm.2013.12.009.

[10]   A. Chanda, R. Mahendiran, Microwave magnetoimpedance and ferromagnetic

resonance in Pr0.6Sr0.4MnO3, RSC Adv. 9 (2019) 29246–29254. doi:10.1039/c9ra06786h.

[11] M. Tejedor, B. Hernando, M.L. Sánchez, V.M. Prida, M. Vázquez, Magneto-impedance effect in amorphous ribbons for stress sensor application, Sensors Actuators, A Phys. 81 (2000) 98–101. doi:10.1016/S0924-4247(99)00095-3.

[12] E. Vremera, C. Fosalau, L. Brunetti, Instrumentation set-up for characterisation of the sensors based on amorphous wires, Meas. J. Int. Meas. Confed. 41 (2008) 327–333. doi:10.1016/j.measurement.2006.11.003.

[13] K.N. Choi, Metal detection sensor utilizing magneto-impedance magnetometer, J. Sensors. 2018 (2018). doi:10.1155/2018/3675090.

[14] A. Sayad, E. Skafidas, P. Kwan, Magneto-impedance biosensor sensitivity: Effect and enhancement, Sensors (Switzerland). 20 (2020) 1–20. doi:10.3390/s20185213.

[15] G.Y. Melnikov, V.N. Lepalovskij, A. V. Svalov, A.P. Safronov, G. V. Kurlyandskaya, Magnetoimpedance thin film sensor for detecting of stray fields of magnetic particles in blood vessel, Sensors. 21 (2021) 1–17. doi:10.3390/s21113621.

[16] J.J. Beato-López, J.M. Algueta-Miguel, C. Gómez-Polo, Contactless magnetic nanoparticle detection platform based on non-linear GMI effect, Meas. J. Int. Meas. Confed. 180 (2021). doi:10.1016/j.measurement.2021.109602.

[17] V.S. Larin, A. V Torcunov, A. Zhukov, M. Vazquez, L.V. Panina, Preparation and properties of glass-coated microwires, J. Magn. Magn. Mater. 249 (2002) 39–45. doi:10.1016/S0304-8853(02)00501-2.

[18] O. Reynet, A.L. Adenot, S. Deprot, O. Acher, M. Latrach, Effect of the magnetic properties of the inclusions on the high-frequency dielectric response of diluted composites, Phys. Rev. B - Condens. Matter Mater. Phys. 66 (2002) 944121–944129. doi:10.1103/PhysRevB.66.094412.

[19] D. P. Makhnovskiy, L. V. Panina, Field dependent permittivity of composite materials containing ferromagnetic wires, J. Appl. Phys. 93 (2003) 4120–4129. doi:10.1063/1.1557780.

[20] I. Liberal, I. S. Nefedov, I. Ederra, R. Gonzalo, S. A. Tretyakov, Electromagnetic response and homogenization of grids of ferromagnetic microwires, J. Appl. Phys. 110 (2011) 1–8. doi:10.1063/1.3631062.

[21] F.X. Qin, H.X. Peng, Ferromagnetic microwires enabled multifunctional composite materials, Prog. Mater. Sci. 58 (2013) 183–259. doi:10.1016/j.pmatsci.2012.06.001.

[22] L. V. Panina, D.P. Makhnovskiy, Magnetic microwires in microwave applications,

656 Elsevier Ltd., 2015. doi:10.1016/B978-0-08-100164-6.00017-5.

[23] 657 A. Allue, P. Corte-León, K. Gondra, V. Zhukova, M. Ipatov, J.M. Blanco, J. Gonzalez,
658 M. Churyukanova, S. Taskaev, A. Zhukov, Smart composites with embedded magnetic
659 microwire inclusions allowing non-contact stresses and temperature monitoring,
660 Compos. Part A Appl. Sci. Manuf. 120 (2019) 12–20.
661 doi:10.1016/j.compositesa.2019.02.014.

[24] 662 M. Peng, F.X. Qin, Clarification of basic concepts for electromagnetic interference
663 shielding effectiveness, J. Appl. Phys. 225108 (2021) 1–9.
664 https://doi.org/10.1063/5.0075019.

[25] 665 H. García-Miquel, M.J. Esbrí, J.M. Andreés, J.M. García, J.M. García-Beneytez, M.
666 Vázquez, Power absorption and ferromagnetic resonance in Co-rich metallic glasses,
667 IEEE Trans. Magn. 37 (2001) 561–564. doi:10.1109/20.914378.

[26] 668 A. Vepsalainen, K. Chalapat, G.S. Paraoanu, Measuring the microwave magnetic
669 permeability of small samples using the short-circuit transmission line method, IEEE
670 Trans. Instrum. Meas. 62 (2013) 2503–2510. doi:10.1109/TIM.2013.2259111.

[27] 671 S. V. Shcherbinin, S.O. Volchkov, A. V. Svalov, V.O. Vas'kovskii, G. V.
672 Kurlyandskaya, Measurement of the parameters of ferromagnetic microwires in a
673 frequency range from 0.1 to 20 GHz, Inorg. Mater. Appl. Res. 11 (2020) 181–187.
674 doi:10.1134/S2075113320010311.

[28] 675 C. Bilzer, T. Devolder, P. Crozat, C. Chappert, S. Cardoso, P.P. Freitas, Vector network
676 analyzer ferromagnetic resonance of thin films on coplanar waveguides: Comparison of
677 different evaluation methods, J. Appl. Phys. 101 (2007) 1–5. doi:10.1063/1.2716995.

[29] 678 E. Fernandez, A. Lopez, A. Garcia-Arribas, A. V. Svalov, G. V. Kurlyandskaya, A.
679 Barrainkua, High-frequency magnetoimpedance response of thin-film microstructures
680 using coplanar waveguides, IEEE Trans. Magn. 51 (2015) 4–7.
681 doi:10.1109/TMAG.2014.2359991.

[30] 682 M. Kilinc, C. Garcia, M. Eginligil, J. Wang, W. Huang, De-embedding zero-field signal
683 in high-frequency magneto-impedance measurements of soft ferromagnetic materials, J.
684 Magn. Magn. Mater. 484 (2019) 424–429. doi:10.1016/j.jmmm.2019.02.021.

[31] 685 J.M. González, A. García-Arribas, S. V. Shcherbinin, V.N. Lepalovskij, J.M. Collantes,
686 G. V. Kurlyandskaya, Broadband ferromagnetic resonance measurements in thin-film
687 structures for magnetoimpedance sensors, Meas. J. Int. Meas. Confed. 126 (2018) 215–
688 222. doi:10.1016/j.measurement.2018.05.070.

[32] 689 A.L.R. Souza, M. Gamino, A. Ferreira, A.B. de Oliveira, F. Vaz, F. Bohn, M.A. Correa,

Directional field-dependence of magnetoimpedance effect on integrated yig/pt-stripline system, Sensors. 21 (2021) 1–12. doi:10.3390/s21186145.

[33] B.C. Wadell, Transmission line design handbook, Artech House Inc, 1991.

[34] G. Crupi, D. Schreurs, Microwave de-embedding: From theory to applications, Academic Press, 2013.

[35] R. El Kammouni, G. Infante, J. Torrejón, M.R. Britel, J. Brigui, M. Vázquez, Microwave behavior in CoFe-based single- and two-phase magnetic microwires, Phys. Status Solidi Appl. Mater. Sci. 208 (2011) 520–525. doi:10.1002/pssa.201026407.

[36] S. V. Shcherbinin, R. Perez, M. Vazquez, G. V. Kurlyandskaya, Ferromagnetic resonance in electroplated CuBe/FeCoNi and amorphous CoFeSiB wires, IEEE Trans. Magn. 56 (2020). doi:10.1109/TMAG.2020.2974141.

[37] D. P. Makhnovskiy, L. V. Panina, D. J. Mapps, Field-dependent surface impedance tensor in amorphous wires with two types of magnetic anisotropy: Helical and circumferential, Phys. Rev. B - Condens. Matter Mater. Phys. 63 (2001) 1–17. doi:10.1103/PhysRevB.63.144424.

[38] M. Knobel, M. Vázquez, L. Kraus, Giant Magnetoimpedance, K.H.J. Buschow (Ed.), Handb. Magn. Mater., 1st ed., Elsevier Ltd, (2003) 497–563. doi:10.1016/S1567-2719(03)15005-6.

[39] Y. Zhao, Y. Wang, D. Estevez, F.X. Qin, H. Wang, X. Zheng, D.P. Makhnovskiy, H. Peng, Novel broadband measurement technique on PCB cells for the field- And stress-dependent impedance in ferromagnetic wires, Meas. Sci. Technol. 31 (2020) 1–8. doi:10.1088/1361-6501/ab4556.

[40] A. Uddin, Y. Zhao, F.X. Qin, On hybrid approach in microwave scattering theory for wire-filled composites, 2021 Photonics Electromagn. Res. Symp., IEEE, Hangzhou, (2021) 528–534. doi:10.1109/PIERS53385.2021.9694931.

[41] S.D. Jiang, T. Eggers, O. Thiabgoh, D.W. Xing, W.D. Fei, H.X. Shen, J.S. Liu, J.R. Zhang, W.B. Fang, J.F. Sun, H. Srikanth, M.H. Phan, Relating surface roughness and magnetic domain structure to giant magneto-impedance of Co-rich melt-extracted microwires, Sci. Rep. 7 (2017) 1–8. doi:10.1038/srep46253.

[42] Rogers Corporation, https://rogerscorp.com/.

[43] Joel P. Dunsmore, Handbook of Microwave Component Measurements: with Advanced VNA Techniques, 2012. doi:10.1002/9781118391242.

[44] GitHub, https://github.com/DYK-Team/vna-impedance-measurments.

724 [45] L.D. Landau, E.M. Lifshitz, Electrodynamics of Continuous Media, Pergamon Press,
725   1975.

726 [46] S. Sandacci, D.P. Makhnovskiy, L.V. Panina, K. Mohri, Y. Honkura, Off-diagonal
727   impedance in amorphous wires and its application to linear magnetic sensors, IEEE
728   Trans. Magn. 40 (2004) 3505–3511. doi:10.1109/TMAG.2004.835676.

729 [47] D. Estevez, Y. Zhao, Y. Wang, F.X. Qin, H.X. Peng, Optimizing magnetoimpedance of
730   amorphous microwires by nanocarbon-induced magnetic anisotropy, J. Magn. Magn.
731   Mater. 502 (2020) 166527. doi:10.1016/j.jmmm.2020.166527.